5-2015

THERMAL POST-FABRICATION PROCESSING OF Y2O3:Tm CERAMIC SCINTILLATORS

Matthew Graham Chapman
Clemson University

THERMAL POST-FABRICATION PROCESSING OF Y_2O_3:Tm CERAMIC SCINTILLATORS

A Thesis
Presented to
the Graduate School of
Clemson University

In Partial Fulfillment
of the Requirements for the Degree
Master of Science
Materials Science and Engineering

---

by
Matthew Graham Chapman
May 2015

Accepted by:
Dr. Luiz G. Jacobsohn (Advisor)
Dr. John M. Ballato
Dr. Colin D. McMillen

Abstract

The effects of thermal post-fabrication processing in O_2 flux on the luminescence and scintillation of Y_2O_3:Tm transparent ceramics were investigated. The material's microstructure, optical properties, and scintillation properties were characterized using X-ray diffraction, attenuated total reflectance Fourier transform infrared spectroscopy, thermoluminescence measurements, differential pulse height distribution measurements, Archimedes density measurements, photoluminescence measurements, and ultra violet-visible transmission measurements. The processing is effective if performed in the time frame of 60-120mins at 1050°C under oxygen flow. After the first hour of processing, about 40% enhancement in the luminescence output together with about 20% enhancement in the scintillation light yield were observed. The enhancements were tentatively assigned to the incorporation of oxygen into vacancy sites. Longer cumulative processing times lead to the incorporation of oxygen as interstitials that is detrimental to scintillation light yield but not to luminescence output. This work also revealed that thermoluminescence measurements are a useful tool to predict scintillation light yield of Y_2O_3:Tm.

Table of Contents

Page

Table of Figures

Page

Table of Figures (Continued) **Page**

Acknowledgements

I would like to begin by thanking my advisor Dr. Luiz G. Jacobsohn for offering his guidance, advice, and support throughout my graduate career. His willingness to provide invaluable insight on the material science academia has served to greatly enhance my learning experience. I would also like to thank Dr. Timothy A. Devol, Dr. Colin D. McMillen, Dr. John M. Ballato, and Dr. Stephen H. Foulger for providing advice, lab equipment, and lab space.

Further, I would like to thank my collegiate associates Matthew Marchewka, Artem Trofimov, Matthew Kielty, and Jaclyn Schmitt for their support and assistance over my graduate career. I wish them the best in their future scientific and academic endeavors.

Furthermore, I would like to thank Clemson University and its Material Science and Engineering department faculty, as well as the electron microscopy staff at the advanced research materials lab for their invaluable aid throughout the duration of my graduate education.

This material is based upon work supported by the National Science Foundation under Grant No. 1207080. A *Minorities in STEM Research Fellowship* from NASA EPSCoR South Carolina Space Grant Consortium for J. M. Schmitt is also acknowledged.

1 – Introduction

1.1 – Scintillation and Scintillators

Detection and measurement of ionizing radiation has become an essential tool in numerous modern branches of scientific and technological endeavor. Much of this detection process, both historical and current, hinges on a process known as scintillation. In essence, scintillation is defined as a material's tendency to luminesce in response to ionizing radiation.

Luminescence refers to the process of light emission from a material that is not a result of blackbody radiation. There are many types of luminescence depending on how a material is excited. These categories and their respective excitation sources include photoluminescence (PL) that uses ultraviolet/visible (UV/Vis) light for excitation, chemiluminescence from chemical reactions, triboluminescence from chemical bond breakage, electroluminescence in response to electrical currents, cathodoluminescence from electron bombardment, thermoluminescence (TL) from heat, and radioluminescence (RL) from ionizing radiation. RL and scintillation are essentially the same, though scintillation is commonly considered the flash of light generated by individual ionizing radiation events, while radioluminescence corresponds to the collective emission of light.

In 1903, Sir William Crookes developed a scintillation detector based on a ZnS screen, called the spinthariscope, which he used to detect and quantify radioactivity. The use of the spinthariscope proved to be valuable in probing the budding field of

radioactivity, but it possessed the crux of a need to physically count the scintillations by direct visual inspection [1]. The development of scintillators stalled until about 1944, when Curran and Baker thought to combine scintillators with the concurrently novel photomultiplier tube (PMT) technology, creating the modern scintillation counter [2]. The invention of PMTs gave researchers a much more efficient device to detect and quantify scintillation. Development of scintillator technology was furthered in 1949, when Robert Hofstadter invented thallium activated sodium iodide (NaI:Tl) that proved to be a phenomenal scintillator [3]. The effectiveness of NaI:Tl single crystals still holds today, as NaI:Tl is even still one of the most commonly used scintillators with the high light yield of roughly 40000 photons/MeV [4]. Scintillators found use in the field of medical imaging with the development of X-ray computed tomography (CT), and positron emission tomography (PET), which are techniques for patient internal imaging that rely on radiation detection [5].

The primary device used for light detection is the photodetector; an instrument that converts UV/Vis light into an electrical signal. Two of the most common photodetector types are PMTs and photodiodes. Some variants of these detectors can reach quantum efficiencies as high as 80% for particular wavelengths of light [6]. However, while both device types excel at detecting radiation within the UV/Vis region of the electromagnetic (EM) spectrum, a shortcoming to both is that they are comprised of materials that are typically low in both density and atomic number. This renders the devices virtually incapable of detecting ionizing radiation due to the lack of effective ionizing radiation stopping power.

Scintillators convert ionizing radiation (i.e., X-rays and gamma rays) into an amplified amount of UV/visible EM radiation, and the pulse of scintillated light can then be detected by the photodetector. Thus, the combination of scintillator and photodetector yields a detector that can produce a significant electronic signal upon interaction with ionizing radiation. Scintillators span the full breadth of material types, with existent variants in both organic and inorganic form, as well as solid, liquid, and gaseous variants. For concision, this thesis will narrow the discussion to inorganic solid scintillators.

Inorganic scintillating solid materials come in the form of single crystals, polycrystalline materials (ceramics), and glasses. An inorganic scintillator can be intrinsic or extrinsic, depending on whether or not the host matrix includes a luminescent dopant known as the activator. Commonly, the activator enhances the scintillation light yield. Typical examples of intrinsic scintillators are $Bi_4Ge_3O_{12}$ (BGO), $CdWO_4$, $CaWO_4$, BaF_2, CeF_3, and CsI. Some of the most prevalent examples of extrinsic scintillators are NaI:Tl, CsI:Tl, LiI:Eu, ZnS:Ag, $Lu_3Al_5O_{12}$:Pr (LuAG:Pr) and CaF_2:Eu, in addition to a number of Ce-doped compounds like the Y, Lu, and Gd oxyorthosilicates ((Y, Lu or Gd)$_2SiO_5$; YSO:Ce, LSO:Ce, and GSO:Ce, respectively), $Y_3Al_5O_{12}$ (YAG:Ce), $LaCl_3$, and $LaBr_3$. This discussion will focus on the extrinsic inorganic scintillators.

A simplified depiction of the extrinsic inorganic scintillation process can be seen in Figure 1. Most inorganic scintillators have an insulating band gap energy above 4-5eV. Thus, there is an appreciable energy difference between the highest energy filled region of the valence band and the lowest energy region of the conduction band. The

region between the two bands, known as the forbidden gap or band gap, is an energy span in which electrons cannot reside as dictated by the basic principles of quantum physics.

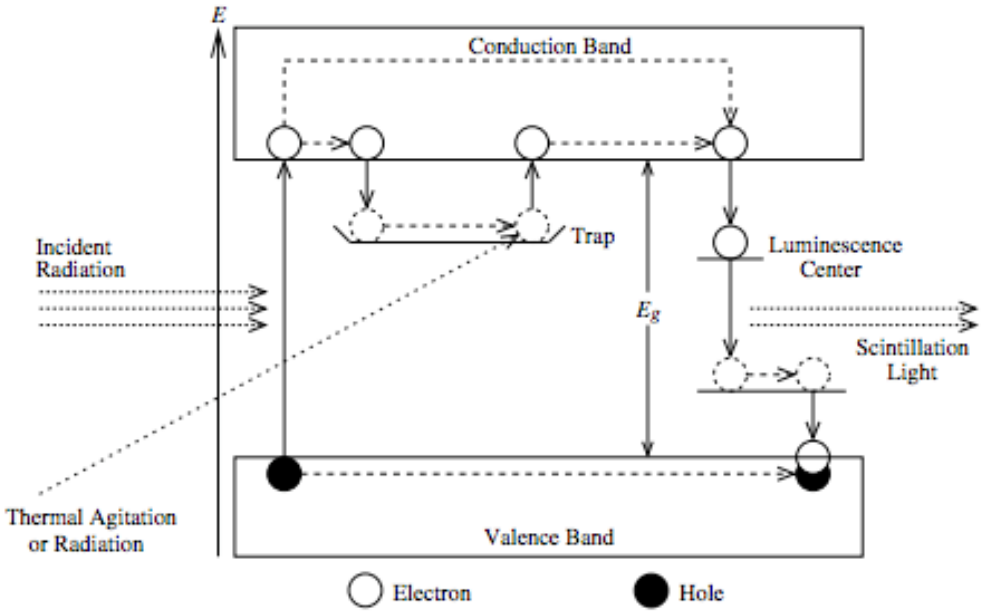

Figure 1: Scintillation band diagram as provided by [7]

There are various energy sources that can impart enough energy into the electrons in the valence band to promote them into the conduction band, thus producing electron-hole (e-h) pairs. A hole is the conceptualization of the positive Coulombic charge density region that remains where the electrically negative electron would normally reside. One such source of excitation is ionizing radiation, a gamma ray for instance. Gamma rays have energies above 100keV, which far exceeds the ionization energy of the matrix-bound electrons. The gamma ray interacts with the electrons in the matrix through one of three mechanisms, namely the photoelectric effect, Compton scattering, and pair

production. However, pair production only occurs for very high gamma energies, and this mechanism is not further considered in this brief introduction. The end result of these interactions is an enormous amount kinetic energy imparted on the electrons of the scintillator. These electrons that directly interact with the ionizing radiation are known as primary electrons. The primary electrons are ejected from the host atoms, and then scatter off of other electrons in the host material, ejecting additional electrons and generating additional e-h pairs. These energized electrons (known as secondary electrons) then proceed to collide with more electrons in the scintillator, and the process repeats in a cascading manner until tens of thousands of electrons are free from their host atoms into the conduction band. This process repeats until the energy of the secondary electrons in the material no longer exceeds the energy threshold required to eject any further electrons from the host material. The number of e-h pairs can be estimated by dividing the energy of the gamma ray by $2.5E_g$, where E_g is the energy of the band gap.

The e-h pairs then proceed to thermalize, a process wherein they lose energy through phonon generation and systemic heat transfer, until the electrons reach the bottom of the conduction band and the holes correspondingly reach the top of the valence band. In some cases, the electron and the hole becomes electrostatically bound to each other, moving through the scintillator as a single entity called an exciton. During their motion through the scintillator, the electrons and/or holes can be captured by traps. These traps correspond to the electronic manifestation of defects in the material that commonly create local energy levels within the band gap, typically within about 1eV from the top of the valence band and below the conduction band. The presence of these

traps is highly detrimental to the scintillation output since they detract from the number of e-h pairs available for radiative recombination.

Excitons are energetically unfavorable and can eventually recombine. If the recombination occurs at the activator, light can be generated. The radiative de-excitation process entails the release of the exciton energy in the form of a photon with energy $E=h\nu$, where h is the Planck's constant, and ν is the frequency of the photon. By quantum mechanical principles, the energy of the photon is equal to the energy difference between the ground and excited states of the de-excitation site. In exact contrast, a non-radiative de-excitation results in the loss of the exciton energy through various other mechanisms that do not produce a photon. Here in lies the end goal of the scintillation process; to de-excite as many excitons as possible in a radiative manner to produce maximum emission of UV/Vis light. These photons then escape from the scintillator, with varying degrees of ease based on the transparency of the host material, where they are then collected by a photodetector device. This concludes the mechanics of the desired scintillation pathway, but there are many other non-radiative pathways that inhibit this mechanism. The main concern of this thesis regards the unwanted defect sites through which the excitons can de-excite non-radiatively.

We will begin by examining the effects of the undesired defects on the electronic band structure. Defects, such as vacancies and interstitial atoms, act as regions of abnormal charge density. These vacancies and interstitial charge abnormalities also introduce localized energy levels into the forbidden gap. These energy levels act as either electron or hole traps in that they provide a means for the electrons and holes to be

captured, thus removing them from the pool of charge carriers that could eventually recombine radiatively. Thus, an important aspect of an efficient scintillator is a low trap density.

In this work, we investigate for the first time the effects of a post-fabrication processing strategy on the scintillation efficiency, with particular attention to its influence on electronic traps.

1.2 – Transparent Ceramics: General Overview

A prominent hierarchy of categorizing inorganic materials revolves around the degree of order in the material. With respect to order, the two extreme groups can be viewed as amorphous and crystalline materials. A crystal is a material that possesses long-range order. An infinite perfect crystalline material can be built from a finite basis of atoms at particular set of spatial coordinates known as the lattice. The unit cell is the smallest structural unit that captures the symmetry of the crystal, and a crystal can be built by translating it in all directions indefinitely. In contrast, amorphous materials do not possess long-range order. The main focus of this thesis is on the crystalline category of this hierarchy.

Crystalline materials can further be broken into two types, single crystals and polycrystalline (ceramic) materials. The single crystal is the basis of the discussion in the previous paragraph, namely an infinitely reproducible singular crystalline structure built up from a repeatable unit cell. A perfect single crystal possesses no internal interfaces.

Ceramics are essentially mosaics of small single crystals; large coagulations of single crystals grains that are randomly oriented throughout the material. The collective behavior of the grains as well as the boundaries where they meet, known as grain boundaries, give rise to many of the unique properties inherent to ceramics.

Single crystals can be optically clear to spectra of light depending on their chemical composition and crystalline structure. With no internal interfaces, the single crystal possesses no internal pores. This is paramount to transparency, because the presence of pores creates local changes of the index of refraction that act as scattering centers.

It was not until the 1960's and 70's when General Electric developed a process to make transparent ceramics in aims to fulfill lighting and lasing applications. They developed a means of pressing ceramics to near bulk density to bring it to a transparent state. They achieved infrared transparency in ThO_2-doped Y_2O_3, which proved useful as transparent ceramic for guided missile windows. Decades later, both Raytheon and GTE were able to improve the transparency of yttria ceramics through the use of hot isostatic pressing (HIP) to get the ceramics to a near-fully densified state without the need for thorium doping [6].

Some recent applications of transparent ceramics include transparent armoring using magnesium aluminate spinel [8], laser media such as YAG:Nd [9, 10], and scintillators such as $(Y,Gd)_2O_3$:Eu,Pr; Gd_2O_2S:Pr,CeF; and $Gd_3Ga_5O_{12}$:Cr,Ce [6]. Some common material types for these different applications are oxide-based materials, including the sesquioxides, spinels, and garnets.

1.3 – Ceramic Scintillators

To explain the motivations of this particular work, we will compare ceramic scintillators with their single crystalline counterparts and elaborate on the advantages and disadvantages of each material type.

Most scintillator single crystals are primarily fabricated in bulk through the Czochralski method, and thus the aspects of single crystal production using this widespread technique will be discussed.

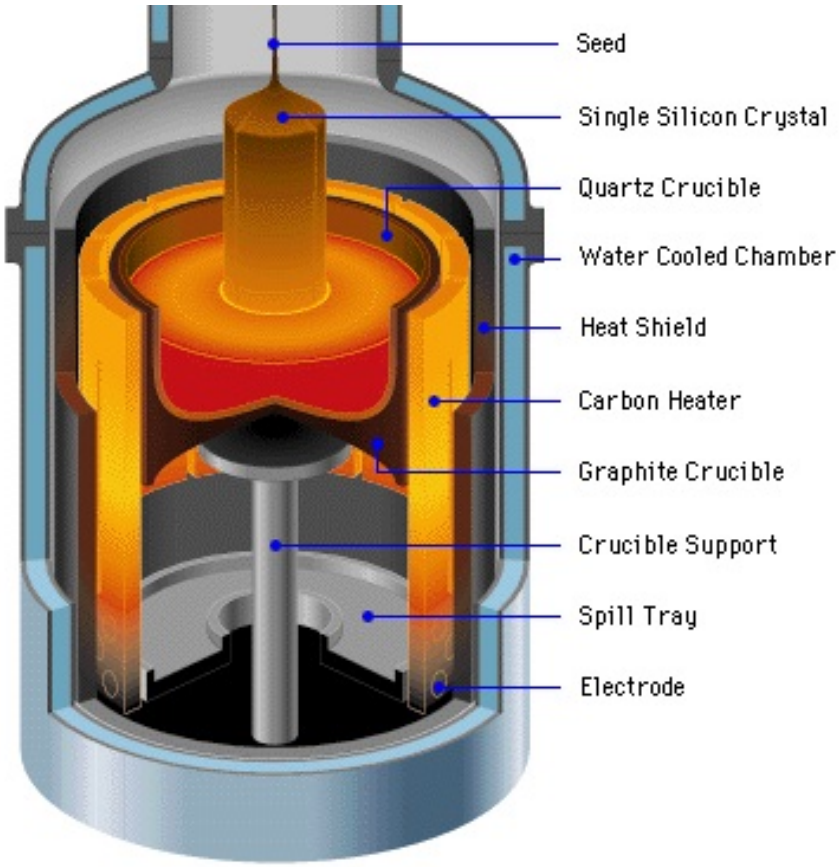

Figure 2: Czochralski method diagram [2]

The Czochralski growth process (seen in Figure 2) begins with a crucible filled with the compound to be crystallized followed by heating until the material within reaches a molten state. A seed crystal is dipped into the molten material, and is then slowly rotated and lifted from the bath forming a crystalline ingot as the material is drawn upwards and cooled below its melting point. This process continues until the ingot has pulled as much material from the bath as possible. It commonly takes 7 to 10 days to grow a single crystal this way.

Single crystals produced through the Czochralski method possess some qualities that are ideal for scintillating materials. They possess a high degree of optical transparency to UV/Vis due to their lack of porosity and defects, and can be grown in relatively large sizes. However, these advantages come with a myriad of pragmatic disadvantages. Single crystals are very expensive to fabricate due to the special working parameters that must be met; the Czochralski method requires that the host material is melted, which can be problematic considering the melting point of some of the desired materials. Yttria, for instance, has a melting point of 2425°C [11], which is not a trivial temperature to achieve. This not only implies that the costs of this method are high, due to specific furnace and crucible requirements, but it further implies that some materials with higher melting points cannot be feasibly made through the Czochralski method. Care must also be taken to manage thermally-induced defects and potential oxidation state reduction due to high temperatures. As pointed out earlier, it takes a relatively long time to grow a crystal. Additionally, Czochralski single crystals can have issues with dopant segregation. Additive dopants within the host material are impurities, and thus it

is often thermodynamically unfavorable for the dopant to be incorporated into the host matrix in relatively large amounts. This can result from additional stress and strain on the matrix due to atomic radii discrepancies, as well as charge mismatch between the host and dopant. As the molten material rises from the crucible and solidifies, the host can lower its energy by ejecting the dopant into the molten material. This both lowers the dopant concentration in the forming ingot and increases the dopant concentration in the bath. The ejection process can result in a concentration gradient of dopant along the length of the final ingot. Since the ingot is typically cut into pieces for use, an inconsistent dopant distribution leads to variation in the quality and performance of the pieces produced.

In contrast, the weaknesses of transparent ceramic scintillators revolve around their optical properties and the fact that the material needs to have a cubic structure, but they possess a suite of advantages over their single crystal counterparts. The typical steps for producing a transparent ceramic involve precursor generation, followed by calcination, sintering, and finally hot isostatic pressing to produce the final product. The ceramic properties will be discussed in regards to this procedure. The specifics of ceramic fabrication will be further discussed in section 2.1.

Transparent ceramics are highly cost effective to produce compared to single crystals. The ceramics require fabrication temperatures considerably lower than the melting temperature. For example, Y_2O_3 transparent ceramics can be sintered at temperatures as low as about 1500°C [12], as opposed to the full melting temperature required during Czochralski single crystal growth. The time required to fabricate a transparent ceramic is

also significantly less than for single crystal fabrication, typically 1-2 days against 7-10 days for single crystal growth. Further, it is easier to have shape control and dopant homogeneity.

One common disadvantage of ceramics is their comparatively lower transparency due to porosity. The second disadvantage is the requirement for cubic crystallographic lattice for any prospective transparent material. Non-cubic crystalline structures exhibit birefringence, which is the anisotropic directionally dependence of the index of refraction. Birefringence is an issue for ceramics, as the random orientation of grains will ensure that the index of refraction constantly changes for light passing through the material. This is not a problem for single crystals, as the entire single crystal is comprised of only one crystalline lattice, thus the entire system has the same orientation. An additional issue for ceramics is that they possess grain boundaries where defects and bond mismatch can exist.

In polycrystalline yttria, a major prevalent defect is the oxygen vacancy. It is expected that these defects create traps in the band gap, which capture electrons and compromise scintillator performance. Enhancement of the performance of transparent ceramic scintillators could further push their use as an attractive alternative to single crystal scintillators, tandem to the goal of this thesis that is to evaluate the effects of post-fabrication thermal processing of transparent ceramics.

1.4 – Y_2O_3:Tm Transparent Ceramic Literature Review

In 1968, gamma-induced low temperature TL of Y_2O_3 and Y_2O_3:rare earth powders, including Y_2O_3:Tm, was investigated [13]. The researchers found that Y_2O_3:Eu possessed the highest TL efficiency among the phosphors, amounting to roughly 10 times the other doped yttria. Y_2O_3:Tm exhibit TL peaks at -155°C, -110°C, and -55°C. The glow curves displayed peaks at 3 and 54°C in Y_2O_3:Sm, Y_2O_3:Eu, and Y_2O_3:Gd that did not exist in Y_2O_3:Tm. This is because the atomic radii of Sm, Eu, and Gd are roughly 1.13Å, which is further away from the atomic radius of Y^{3+} (atomic radius is 1.06Å) than the Tm^{3+} ion (atomic radius is 1.04Å). The group found the primary emission band from Y_2O_3:Tm to be 453nm.

The optical constants of Y_2O_3 single crystals were explored through infrared spectroscopy and UV/Vis transmittance in 1968 [14]. This group observed an optical transparency window between 250 to 9600nm, and found the transparency cutoff wavelength to be 220nm. Infrared spectroscopy revealed that the yttria crystal lattice had two primary absorption centers at about $436cm^{-1}$ and $390cm^{-1}$, with several other absorption lines from 560 to $120cm^{-1}$.

TL was investigated as a possible technique to identify secondary phases of various materials that can appear due to high temperatures needed in the fabrication of superconductors, including Y_2O_3, Y_2BaCuO_5, $BaCO_3$, Ba_3CuO_4, and $BaCuO_2$ [15]. Gamma and X-ray excitation of Y_2O_3 yielded TL peaks at 115°C, 190°C, and of the tested materials, Y_2O_3 had the highest TL intensity.

Garnier et al. assessed upconversion and photon-avalanche absorption from nanocrystalline Y_2O_3:Tm prepared by the combustion method, noting the excited state absorption at 654nm, and the large emission around 470nm from $^1D_2$ to $^3F_4$ transitions [16].

The potential of Y_2O_3:Tm for application as a diode-pumped laser material was investigated by Ermeneux et al. [17]. The emission spectra of the Y_2O_3:Tm was recorded around 1.5μm corresponding to Tm^{3+} $^3H_4$ to $^3F_4$ transition. The authors investigated the 800nm broadband emission that stems from the $^3H_6$ to $^3H_4$ optical transition. The researchers also found a sharp emission at 1550nm unique to Y_2O_3:Tm resulting from $^3H_4$ to $^3F_4$ transitions. This emission is of interest due to its safe infrared wavelength for lasing application.

Y_2O_3 undoped and Tm^{3+} doped single crystals were grown through the micro-pulldown method and the thermal diffusivity and conductivity were investigated by Mun et al. [18]. Values of undoped Y_2O_3 thermal diffusivity and conductivity were obtained as $7.2*10^{-6}m^2s^{-1}$ and $15.94Wm^{-1}K^{-1}$. For the 5% Y_2O_3:Tm, the thermal conductivity drops to $8.34Wm^{-1}K^{-1}$. This group additionally studied the 2μm infrared emission of the Y_2O_3:Tm with decay time 3.08ms, from $^3F_4$ to $^3H_6$.

Control of grain size growth of 1% Y_2O_3:Tm transparent ceramics using ZrO_2 and tetraethyl orthosilicate (TEOS) as additives was reported by Li et al. [19]. The authors succeeded in retaining grains with sizes around 20-30μm and high transmittance at 2μm with ZrO_2.

The effects of different sintering atmospheres have been investigated by Yihua et al. [20], in which sintering was carried out in an oxygen environment to achieve grain sizes that were less than one micron. Yttria ceramics are typically sintered in vacuum in order to eliminate the pores during grain diffusion. Pore elimination is hampered by sintering in air because the nitrogen molecules, which comprise 79% of air, are too large to diffuse through the material. The evacuation of nitrogen causes stress cracks to form in the final product. This group studied the outcomes of sintering in O_2, theorizing that the oxygen would diffuse through the material more easily, thus allowing for non-destructive reduction of pores. They produced transparent samples after sintering at 1600°C with grain sizes smaller than one micron.

Y_2O_3:Tm was chosen to be investigated in this work because know-how on making transparent ceramics of this material was available at COMSET, together with reasonable ionizing stopping power from Y_2O_3 and blue emission from Tm^{3+} dopant.

2 – Experimental Procedure

2.1 – Samples

2.1.1 – Y_2O_3:Tm Transparent Ceramic Fabrication

Fabrication of the ceramics follow the procedure developed at COMSET[12, 21]. It began with synthesis of the precursor nanopowder through a coprecipitation reaction between ammonium hydroxide and yttrium nitrate solution. In the case of Tm-doped yttria, the yttrium nitrate solution consisted of yttrium nitrate hexahydrate (99.9% purity, Acros Organics) and thulium nitrate hydrate (99.9% purity, Acros Organics), both dissolved in ultrapure water, with the stoichiometric ratio of the two compounds such that a 0.5% molar substitution of Tm for Y was used to optimize luminescence[22]. For the investigation of the effects of the sintering temperature, undoped yttria ceramics were prepared, i.e. no thulium nitrate hydrate was added to the yttrium nitrate hexahydrate solution. The 2M ammonium hydroxide solution (Certified A.C.S. Plus, Fisher Scientific) was mixed with 5mol% ammonium sulfate (99.99% purity, Sigma Aldrich). This ammonium solution was dripped into the nitrate solution to slowly precipitate the nitrate precursor compound. The precipitate was agitated over a 3hr period at room temperature, and then washed four times in centrifuge; twice in ultrapure water, and then twice in ethanol. The cleaned precipitate was then dried overnight in a vacuum oven at 60°C. After drying, the precursor powder was calcined for 4hrs at 1050°C under oxygen flow at 3l/min. The end result was a Y_2O_3:Tm nanopowder. The powders were then

mechanically pressed into pellets under 15MPa in the absence of any binding agents. The pellets were then cold isostatically pressed at 206MPa to stabilize the pellets. For the fabrication of undoped yttria ceramics, sintering was carried out at a single temperature, from 1400 to 1700°C, for 20hrs in air ("one-step" method). For the fabrication of Y_2O_3:Tm transparent ceramics, two-step sintering was used, first by heating the pressed pellets to 1500°C at a heating rate of 10°C/min followed by an immediate cooling to 1400°C in vacuum. The pellets were held at 1400°C for 20hrs to achieve dense, still opaque, sintered ceramic pellets. Transparency was then achieved through hot isostatic pressing at 1300°C for 3hrs under pressurized argon gas at 206MPa, followed by polishing to optical grade. The samples used in this thesis were the result of previous work of student Steven A. Roberts at COMSET [12, 23].

2.1.2 – Post Fabrication Processing

The investigation of the effects of thermal post-fabrication processing of the transparent ceramics was carried out as follows. First, the sample was processed at 1050°C under O_2 flow for up to 10hrs total, with breaks at 1, 2, and 5hrs of cumulative processing. Characterization was carried out at each break in the thermal processing. The sample was processed in a zirconia boat in a box furnace in such a way that both surfaces of the sample were exposed to O_2 flow. The characterization techniques performed at each step included photoluminescence, thermoluminescence, and differential pulse height distribution measurements. Additionally, X-ray diffraction, density, attenuated total reflectance Fourier transform infrared spectroscopy, and optical

transmittance measurements were performed for both the pristine and 10hr processed sample. These techniques and their measurement procedures are described in detail below.

2.2 – Characterization Techniques

2.2.1 – X-ray Diffractometry

X-ray diffractometry (XRD) is a leading technique in characterizing the crystalline structure of materials. The core of XRD entails treating the crystal structure as an atomic diffraction grating. Diffraction describes the interaction between EM radiation and slits. If the spacing of the slit is comparable to the wavelength of incident light, then the light will propagate from the slit as a spherical wave front as dictated by the Huygens-Fresnel principle (Figure 3).

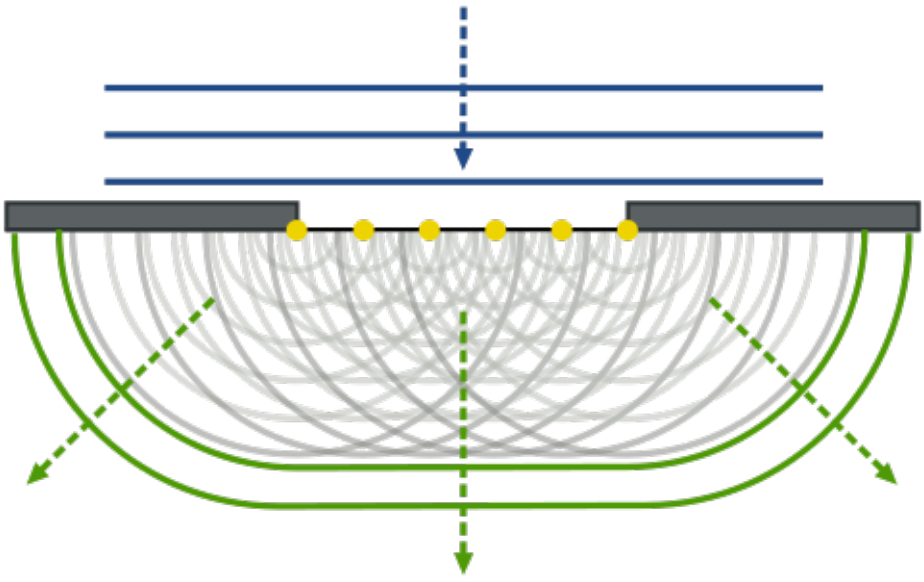

Figure 3: Huygens-Fresnel spherical wavefronts as provided by [24]

Multiple spherical wave fronts can overlap to create regions of destructive and constructive interference, creating intensity minima and maxima. The periodic pattern created is known as a diffraction pattern. As discussed in section 1.2, a perfect crystal has periodicity from the repetition of the unit cell. This periodicity gives the crystal a system of planes where atoms are distributed within. These planes have consistent spacing that depends on the lattice parameters of the unit cell. XRD hinges on using the distance between these planes as diffraction slits. The diffraction pattern that emerges from atomic slits is dictated by Bragg's law:

$$n\lambda = 2dsin\theta \quad (1)$$

where n is an integer denoting the diffraction maxima, λ is the wavelength of incident light, and θ is the angle of incidence. The maximum constructive interference between the two waves occurs at a phase difference of nλ, and destructive intereference is at a maximum when the phase difference is nλ/2. In practice, the only diffraction maximum of interest is the primary one, and thus we are only concerned with the case of n=1.

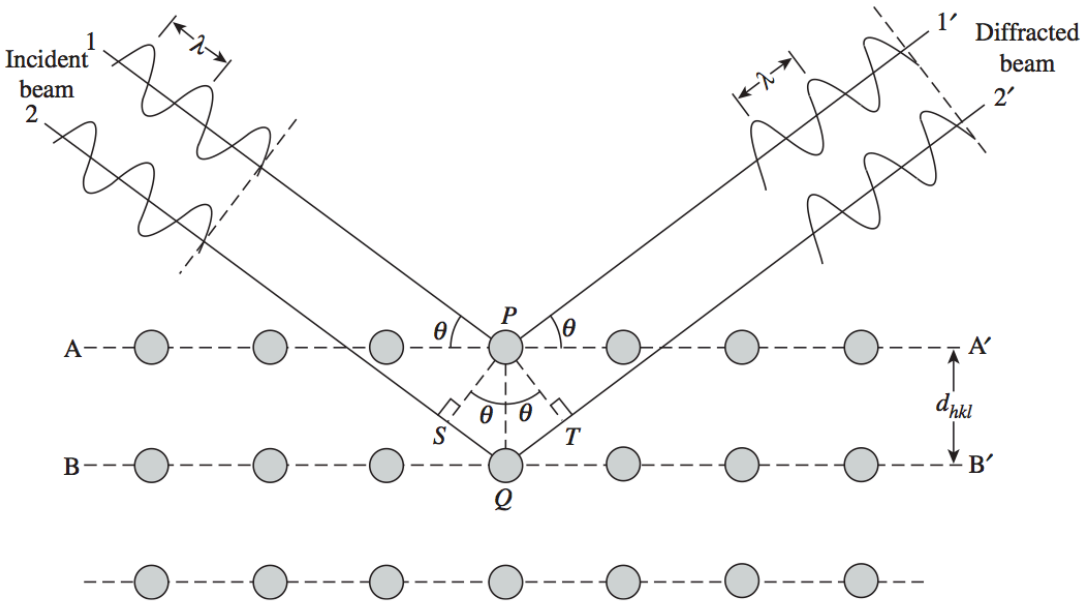

Figure 4: Bragg's law of diffraction diagram as provided by [25]

In the case of the cubic materials the lattice parameter, a, and a given crystalline plane defined by the Miller indices h, k and l are related through:

$$d_{hkl} = \frac{a}{(h^2+k^2+l^2)^{\frac{1}{2}}} \tag{2}$$

We can combine equations for Bragg's law with atomic spacing to yield a relation between the lattice parameter and the angle of radiation incidence.

$$a = \frac{n\lambda(h^2+k^2+I^2)^{\frac{1}{2}}}{2sin\theta} \tag{3}$$

As mentioned before, EM radiation must be of comparable wavelength with the atomic spacing in order for diffraction to occur. Thus, X-rays are used for atomic diffractometry, as the average atomic spacing falls within the X-ray wavelength range.

X-ray diffractometers generate X-rays by accelerating high-energy electrons into a metallic target, typically copper.

An X-ray diffractometer contains essentially 2 components; the X-ray source and the X-ray detector. The process begins with the Cu Kα and Kβ X-rays generated in the X-ray tube. The X-rays pass through the Soller slits and are collimated, and then travel to the sample. After the sample diffracts the incoming X-rays, the detector is oriented such that it will gather the diffracted rays. In the common Bragg-Brentano arrangement, the detector is mounted on a rotary track that allows it to sweep through the 2theta domain to build the intensity profile, where theta is the irradiation angle. Theta and 2theta are systematic varied simultaneously. Before the diffracted X-rays reach the detector, the X-rays pass through a monochromameter and anti-scattering slits to ensure a signal beam of monochromatic X-rays (i.e. Kβ is eliminated) reaches the detector. This maximizes the technique resolution in achieving a heightened degree of diffraction peak centroid accuracy.

Figure 5: The Rigaku Ultima IV X-ray diffractometer

The XRD measurements were accrued with a Rigaku Ultima IV X-ray diffractometer model (Figure 5) using 40kV acceleration voltage and Cu Ka+Kβ radiation. The sample was placed in the center of a low X-ray scattering background silicon holder. The sample was scanned over a 45° range from 15 to 60 degrees with a 0.01° angular resolution at a scanning rate of 1°/min. Peak centroids were located through the PDXL XRD software using the 2nd derivative method.

2.2.2 – Density Measurements (Archimedes method)

An important parameter of interest with transparent ceramics is the density of the ceramic material relative to bulk density. As mentioned in section 1.2, ceramics commonly contain grain boundaries and pores that reduce the average density and optical transparency. The pores contain pockets of air, which change the local index of refraction relative to the bulk material and act as effective scattering centers, being a negating factor for transparency. Thus, a major portion of the advances in transparent ceramic technology involves maximal densification through the elimination of pores to optimize transparency. One simple method of tracking density is through application of Archimedes principle.

The basis of the Archimedes principle is that an object immersed in a fluid will experience a buoyant force equal to the weight of the liquid displaced. The buoyancy force is a result of the pressure applied by the liquid against the object. Since the magnitude of the pressure depends on the surface area of an object, two objects with the same mass but different volumes will experience different buoyancy forces. This implies that the density of a material will affect the pressure it suffers when immersed weight in a liquid. Noting the difference in weight of a material in a known liquid is the basis of using Archimedes principle to determine an object's density.

One method of using Archimedes principle is by saturating the ceramic with water. Submerging the ceramic in water for an extended period of time allows for water to diffuse into the pores of the material. A comparison of the mass of the ceramic

saturated with water versus oven dried can yield the density of the sample through the relation:

$$D_{Sample} = D_{Water} \frac{M_{dry}}{M_{Sat} - M_{IW}} \quad (5)$$

where D_{sample} is the sample density, D_{Water} is the density of water, M_{dry} is the dry mass, M_{sat} is the saturated mass, and M_{IW} is the mass of the sample in water.

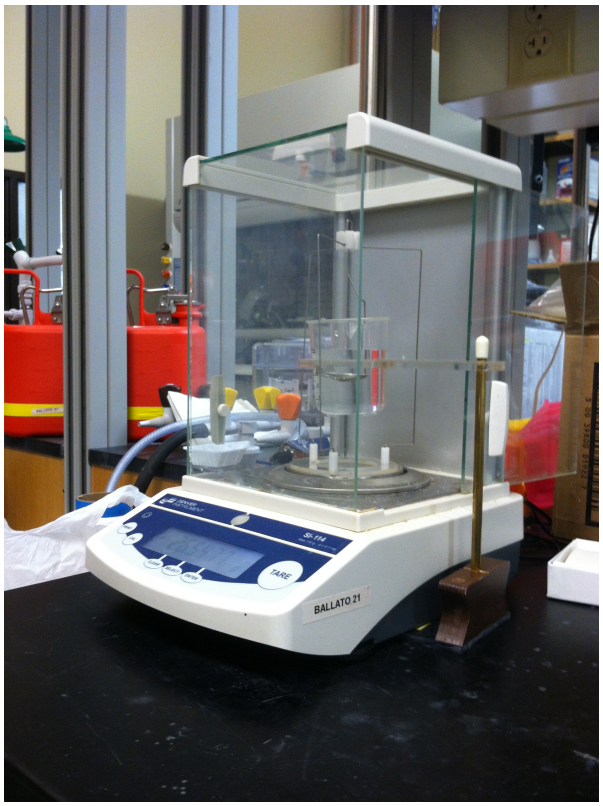

Figure 6: Universal specific gravity kit, bench model SGK-B

Preparation for the density measurements began with soaking the samples for 24hrs in ultrapure H_2O under vacuum. The samples were then weighed in water on the Archimedes density platform (Figure 6) to obtain M_{IW}. They were then removed from

the water, the surfaces were dried, and then the mass was again recorded (M_{sat}). The samples were then placed to dry at low temperature in a furnace for 24hrs, and were weighed (M_{dry}). The M_{IW} and M_{sat} were measured a total of five times each, and the dry mass was measured once. Average values for the sample were calculated.

2.2.3 – Positron Annihilation Spectroscopy (PAS)

Positron annihilation spectroscopy is a useful technique to assess the porosity of a material. It accomplishes so by injecting positrons in a material and recording the resulting gamma ray emission.

A positron is the oppositely charged antiparticle to the electron. As such, an electron-positron collision results in matter-antimatter annihilation, which produces gamma rays with energies of 0.511MeV, the rest energy of the electron and positron. The time of initial positron emission is recorded by tracking gamma rays that are released as products of the positron decay. A common example of a positron emitter is ^{22}Na, which releases a positron and a 1.27MeV gamma ray roughly 10ps later. The positron lifetime within the solid varies greatly depending on the porosity of the material.

The atoms in the matrix are comprised of dense positively charged nuclei surrounded by negative electron clouds. The dense positive core of the atom is a repulsive Coulombic potential spike for the positron passing through. When vacancy defects occur, the dense positive nucleus is absent from the site, and thus the vacancy acts as a minimal energy point for a positron (Figure 7).

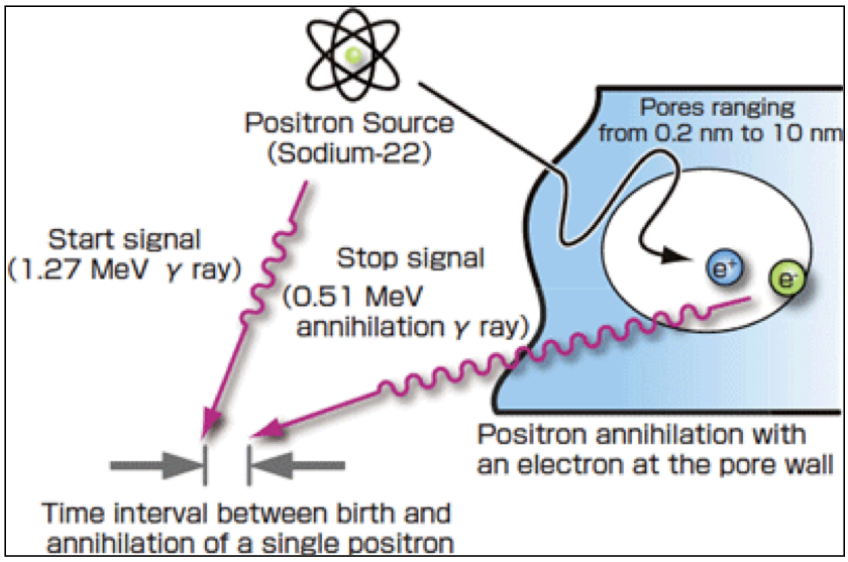

Figure 7: Positron annihilation spectroscopy general overview

As a result, the positron can become trapped in a vacancy for a relatively long duration. This leads to distinct lifetimes of positrons injected into a material; the positron can either annihilate in the bulk with lifetimes of a few 100ps, or it can stabilize in a pore and survive on the order of up to a few ns, depending on the size of the pore. Assessment of porosity by means of lifetime analysis is known as the positron annihilation lifetime (PAL) technique [26].

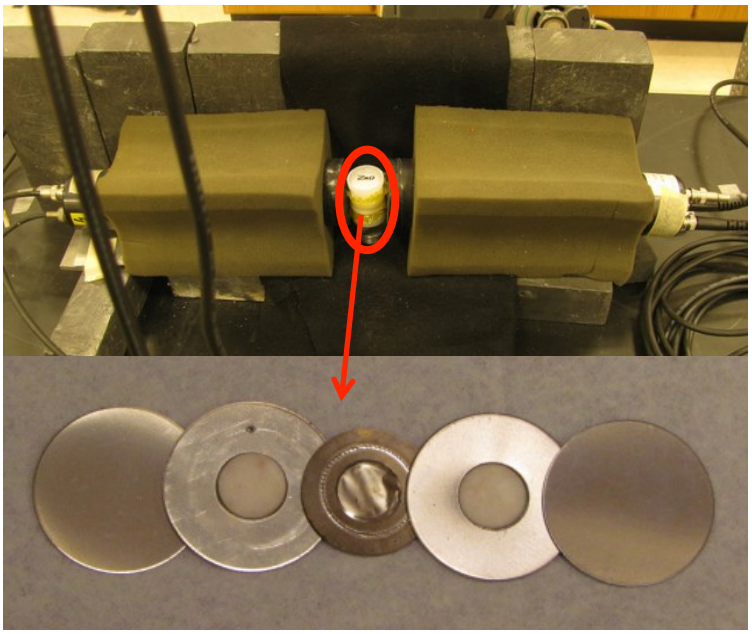

Figure 8: PAS experimental setup

PAS measurements were carried out by Professor C.A. Quarles with the Department of Physics and Astronomy, Texas Christian University. PAL was measured in a typical fast-fast coincidence set-up using the 1.27MeV gamma ray from the ^{22}NaCl source for the start signal and the 0.511MeV annihilation gamma ray for the stop signal (Figure 8). Lifetime runs were made to obtain 1 to 8 million events total. The lifetime data were analyzed with the program LT (version 9) [27].

The Doppler broadening experiment was done with a ^{68}Ge source using a liquid nitrogen cooled high purity germanium detector (HPGe). Data were collected to obtain 4 million events in the 0.511MeV peak. The analysis of the Doppler broadening spectrum was done with the Sigma Plot software using an analysis program that analyzes the Doppler broadened 0.511MeV annihilation gamma-ray and determines the S and W

parameters for the peak. The S parameter was defined as the ratio of the number of counts within about 1keV of the 0.511MeV peak center to the total number of counts in the peak, while the W parameter corresponded to the ratio of the number of counts in the wings of the peak to the total number of counts in the peak.

2.2.4 – ATR-FTIR

Fourier transform infrared spectroscopy (FTIR) is a widely used technique for chemical analysis and bond structure assessment. The sample is irradiated with a spectrum of infrared radiation, and frequencies that match the resonant frequency of atomic bonds will be absorbed. The frequency pattern of absorption is chemically dependent, which allows for identification of the chemical nature of the vibrating group.

An FTIR spectrometer is primarily comprised of a Michelson interferometer (Figure 9) and infrared radiation source.

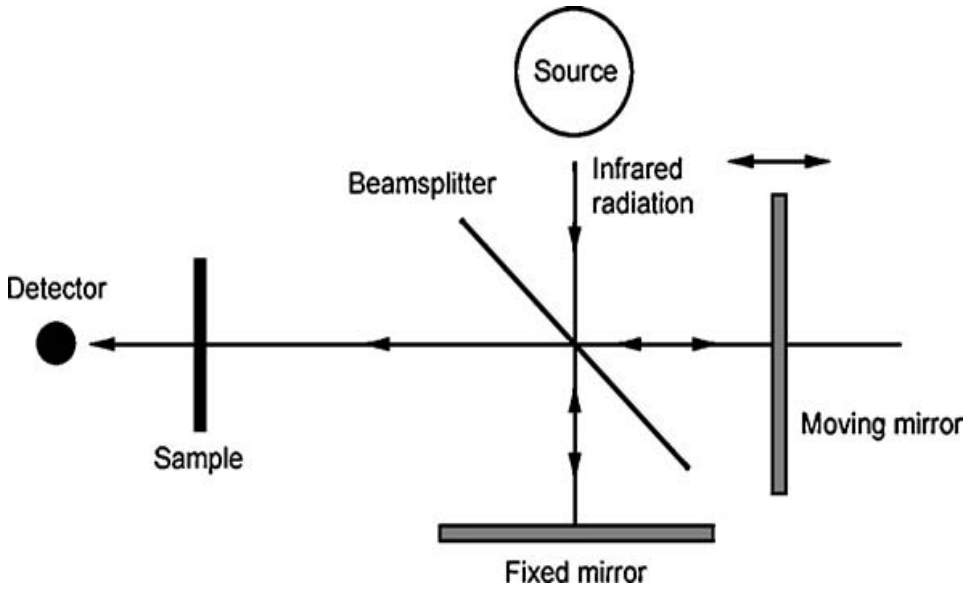

Figure 9: Michelson interferometer as provided by [25]

The interferometer consists of a beam-splitter and two mirrors, one of which is mobile. The infrared spectrum encounters the beam splitter and half of the radiation is reflected towards the mobile mirror while the other half is transmitted through to the fixed mirror. The radiation from each mirror then is reflected and transmitted again, recombining to irradiate the sample and then pass to the detector. The moving mirror is spaced from the splitter such that it there is an optical path length difference, δ, between the two mirrors relative to the splitter. This results in constructive and destructive interference. The interference intensity as a function of path difference is gathered to form an interferogram. This interferogram is comprised of convoluted sinusoidal intensity curves, which can be Fourier transformed to give an intensity versus infrared spectrum. The absorption peaks of the resulting spectrum correspond to the wavenumber of the vibrational modes in the material.

In conventional FTIR, the radiation is passed straight through the sample for collection. In the case of attenuated total reflection Fourier transform infrared spectroscopy (ATR FTIR), the infrared radiation is totally internally reflected through an ATR crystal in contact with the sample. The internally reflected radiation produces evanescent waves within the sample that pass through to the detector.

Figure 10: Thermo-Scientific Nicolet 6700 FTIR spectrometer

ATR FTIR was performed on the as fabricated short and long term processed samples using the Thermo-Scientific Nicolet 6700 FTIR spectrometer (Figure 10) with a diamond crystal ATR plate. FTIR spectra were gathered from 400 to 4500cm^{-1} at 100 scans with a spectral resolution of 1cm^{-1}.

2.2.5 – UV/Vis Spectroscopy

The scintillation light yield of a transparent ceramic is highly dependent on the transparency to the light emitted from the activators (luminescence centers). Since the scintillated light is UV/Vis light, it is important to inspect the UV/Vis transparency of the material.

As discussed in section 1.1, the band structure of the ceramic consists of a forbidden energy gap between the valence band and conduction band. Quantum physics dictates that electrons cannot exist at energies within the band gap. This property of the band gap dictates the material's ability to interact with light.

The absorbance A of light passing through a material at an initial intensity I_0 is defined as:

$$A = \log_{10}\left(\frac{I_0}{I}\right) \tag{7}$$

where I is the intensity of light that passed through the material. The UV/Vis spectrophotometer acquires the absorbance for the material as a function of wavelength to generate an absorbance spectrum. Alternatively, it can acquire data as transmittance that is defined as I/I_o.

Figure 11: Perkin Elmer Lambda 950 UV/Vis/NIR spectrometer

The optical transparency of the ceramics was measured with the Perkin Elmer Lambda 950 UV/Vis/NIR spectrometer (Figure 11). Transparency data was gathered over the wavelength range of 200-2000nm with a wavelength resolution of 1nm.

2.2.6 – Photoluminescence

It is important to assess the luminescence centers in the scintillating material. A leading method for this assessment is photoluminescence spectroscopy (PL). This entails excitation of the luminescent centers with UV and visible light to prompt the emission of light with longer wavelength (lower energy) from the activators.

A key requirement for an optimal luminescent center is a high probability of radiative de-excitation. Rare earths are known to be efficient activators, with the energy of the emitted photon being within the UV/Vis/NIR region of the spectrum. From a quantum physical perspective, electrons should only be excited from photons matching the exact difference in energy between the ground and excited states. However, vibrational modes provide additional energy states above the excited states, allowing for excitation from a narrow range of photon energies. Once excited to a higher vibrational mode, the excess energy is dissipated to the surrounding matrix through phonon generation such that the electron is now at the lowest vibrational state associated to the excited electronic state. From there, the electron de-excites to some vibrational level related to the ground state. Again, the excess energy is dissipated to the surrounding matrix through phonon generation such that the electron is moves to the lowest vibrational state associated to the ground state. As a result, the photon emitted from the de-excitation process will have lower energy than the excitation photon. This phenomenon is known as the Stokes shift.

Photoluminescence spectroscopy involves exciting the luminescent centers and recording the resulting emission as a function of wavelength. The controlling factor for the emission intensity and wavelength are the chemical nature of luminescence center and its electronic interaction with the host matrix. The presence of quenching defects at the close vicinity of a luminescence center can affect its emission efficiency.

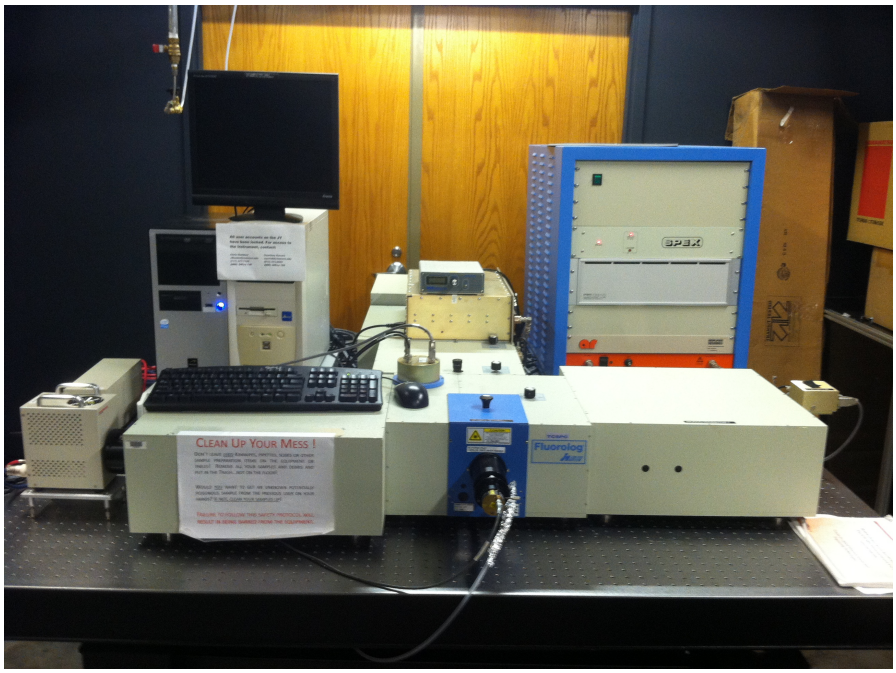

Figure 12: Horiba Jobin-Yvon Fluorolog-322 spectrofluorimeter

PL measurements were carried out with a Horiba Jobin-Yvon Fluorolog-322 spectrofluorimeter (Figure 12) in the double grating configuration. Both the source and detector were angled 45° relative to the sample face. Samples were excited at 360nm and emission was recorded in the 390-500nm range with a spectral resolution of 1nm and integration time of 0.5s.

2.2.7 – Thermoluminescence

Thermoluminescence is the emission of light upon heating that is not related to blackbody radiation. For thermoluminescence to occur, it is necessary for a material to contain traps within the band gap and a luminescence center.

The thermoluminescence mechanism will be described in terms of the electron behavior, though an equivalent rationale can be applied for the hole. Once an electron is thermalized at the bottom of the conduction band, as described in section 1.1, it can be captured by traps within the band gap. If the energy difference between the trap level and the conduction band is large enough, the trapped electron can be contained for long amounts of time.

During a TL measurement, the sample is heated up to progressively provide thermal energy until the electron is able to leave the trap and be promoted to the conduction band. From there, it can either recombine at the luminescence center with the emission of light, or fall back to the trap. Glow curves are obtained in the form of emission intensity as a function of temperature.

Figure 13: Thermo Scientific Harshaw TLD reader model 3500

TL measurements were performed with a Thermo Scientific Harshaw thermoluminescence dosimeter (TLD) reader model 3500 (Figure 13). Samples were heated from 50 to 400°C at a rate of 5°C/s and held at 400°C for 5mins in order to completely deplete the traps. The sample was then immediately measured from 50 to 400°C at a rate of 5°C/s with no annealing to verify that the traps were fully depleted in the previous run. The samples were then irradiated with ^{137}Cs for 180s and then measured from 50 to 400°C at a rate of 5°C/s. The glow curves for each processing step were integrated and plotted as a function of processing time.

2.2.8 – Differential pulse height distribution measurements

Differential pulse height distribution measurements (subsequently referred to as light yield measurements) determine the scintillation relative brightness of the ceramic in relation to a known reference.

In a photomultiplier tube, photons from the scintillator eject photoelectrons from a material with low work function known as the photocathode. The photoelectron is then accelerated down an electrical potential voltage, which is obstructed by dynodes. The photoelectron ejects secondary electrons from the dynodes, which proceed to further eject electrons from dynodes further down the potential gradient. This effect cascades until the end result is a single photon converted into a measurable electrical signal. The intensity of the electrical signal is proportional to the number of photons emitted from the scintillator and the energy of the ionizing radiation. Therefore, for a same radioactive source, the ratio of the electrical signal size between the sample and reference provides the relative brightness of the sample. In practice, the electrical signal is collected by a multi-channel analyzer, where the channel corresponding to the maximum of the distribution is extracted and used for determining the brightness ratio. In differential pulse height distribution measurements, the scintillator brightness is correlated to the channel number of the photopeak; the higher the peak channel number, the brighter the material.

Figure 14: Hamamatsu R6095 bialkali photocathode photomultiplier tube

The setup for light yield measurements involved coupling the sample to photomultiplier tube with an optical grease. Samples were measured in reference to a BGO single crystal using a Hamamatsu R6095 bialkali photocathode photomultiplier tube (Figure 14) with a 1000V operating voltage under irradiation from an alpha blocked ^{241}Am source for 60s. The BGO crystal was measured in the same manner as the samples. The photopeaks were fit with Gaussian curves to find the peak centroids. The ratio of the centroids yielded the sample light yield in relation to the light yield of BGO.

3 – Results & Discussion

3.1 – Sintered Y_2O_3 Series

Before discussing the effects of post-fabricaton processing, it is useful to examine the effects of sintering on the trap content of the material. Figure 15 compares the TL glow curves of calcined and calcined + sintered Y_2O_3, and illustrates the differences between them. It is clear that the glow curve from the calcined sample contains additional traps compared to the sample that was calcined and sintered, as exhibited by the intense emission centered at about 150 and 250, and above 350°C that possibly corresponds to the onset of a glow peak beyond the detection limit of the equipment. From this perspective, sintering seems to be beneficial in eliminating electronic traps from the material, though the identity of the traps is unknown.

In Figure 16, the effects of sintering temperature on mass normalized TL emission are reported. Glow curves are composed by a dominant peak centered at about 110°C, together with a significantly weaker peak centered at about 320°C. While the glow curve shape of the sintered samples remains unchanged, suggesting that no new types of traps were created, TL intensity increases as a function of sintering temperature, with the largest increase occurring between 1600 and 1700°C (Figure 17).

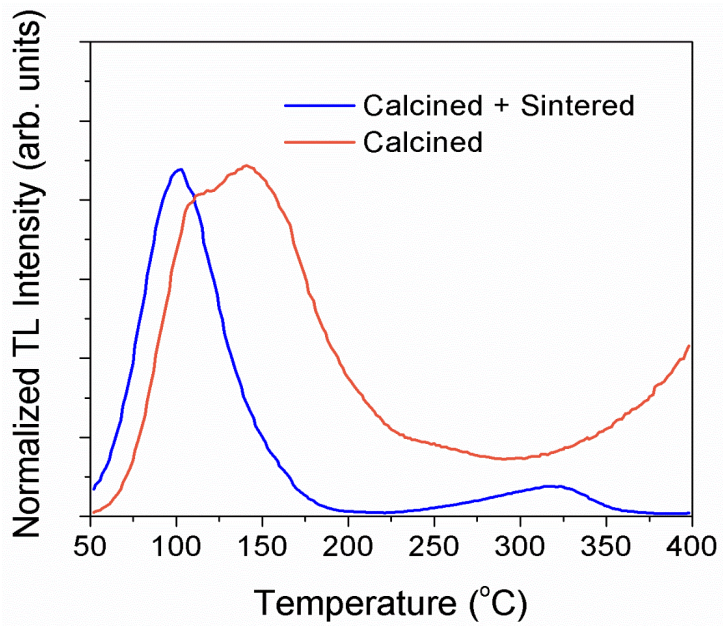

Figure 15: Normalized TL intensity of calcined and 1400^{0}C sintered samples

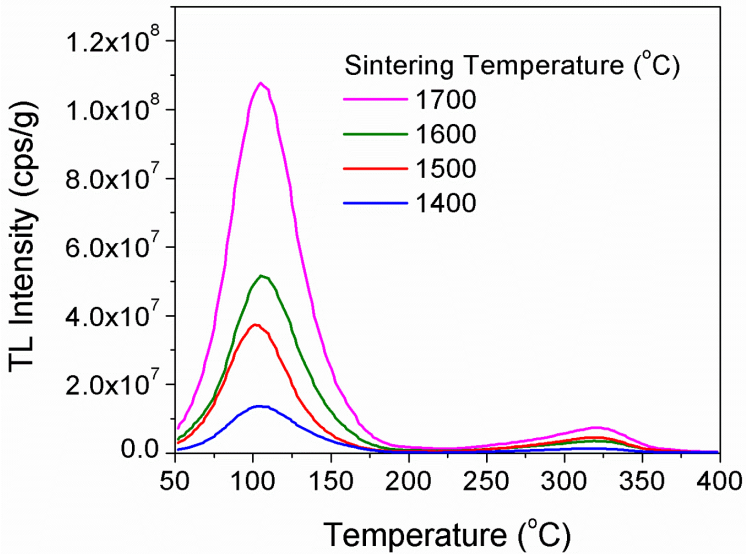

Figure 16: Representative mass-normalized TL glow curves of Y_2O_3 sintered at 1400, 1500, 1600, and 1700^{0}C

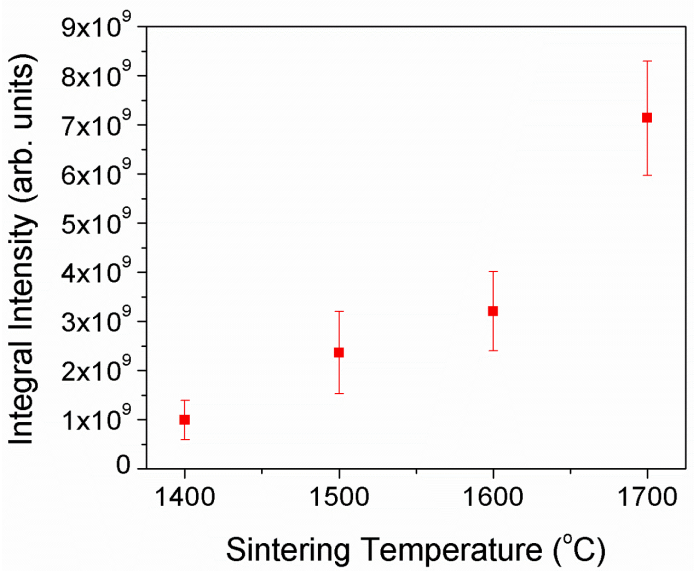

Figure 17: Integral TL intensity as a function of sintering temperature. Each glow curve was normalized by mass before integral intensity was extracted

As expected, sintering also has a significant effect on the density of the ceramics (Figure 18). The density results show that a minimum sintering temperature of 1450°C is required to reach about 99% bulk density.

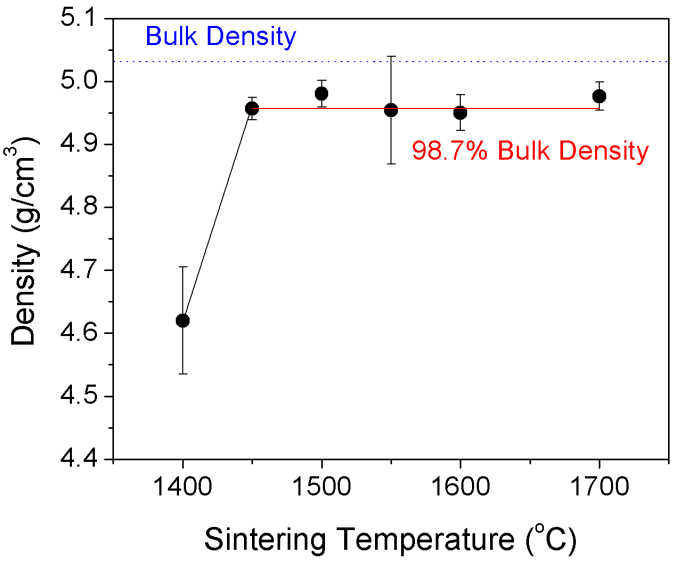

Figure 18: Density as a function of sintering temperature

Consolidation was further investigated by means of positron annihilation spectroscopy. Analysis of PAL data revealed the presence of two lifetimes, one around 200ps and the other within 1 to 4ns as can be see in Figure 19. The relative intensities of the positron annihilations corresponding to these lifetimes are shown in Figure 20. These results show that the interaction of positrons with the sample is dominated (>99%) by annihilations with "bulk" electrons with a small contribution coming from open-volume defects (<1%). Thus, PAL measurements concur a reduction in porosity as sintering temperature increases.

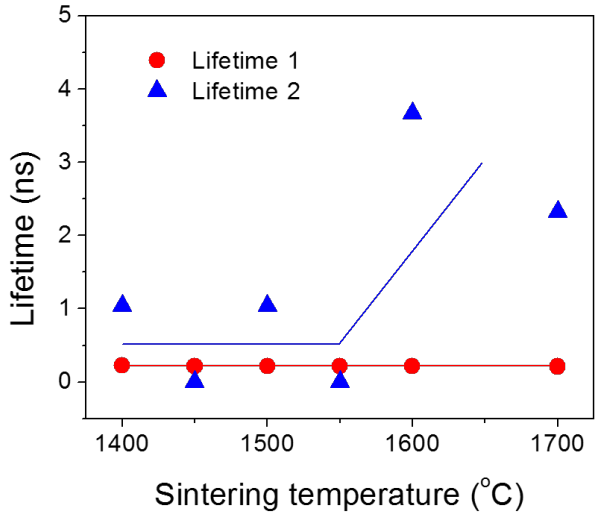

Figure 19: Lifetime of long-lived positrons as a function of sintering temperature

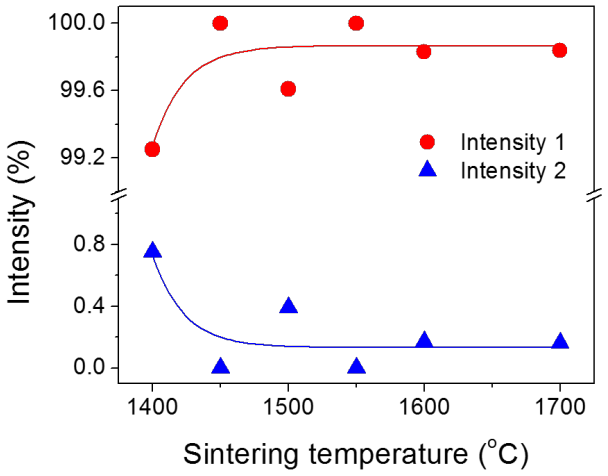

Figure 20: Intensity of short (intensity 1) and long (intensity 2) positron decay lifetimes

On the whole, there is a high degree of densification and reduction of porosity together with the elimination of some type of traps for higher sintering temperatures, but at the cost of increasing the concentration of the remaining traps.

3.2 – Post-Fabrication Processing

XRD results confirmed the single phase cubic structure for the processed sample in accordance to JCPDS card #41-1105.

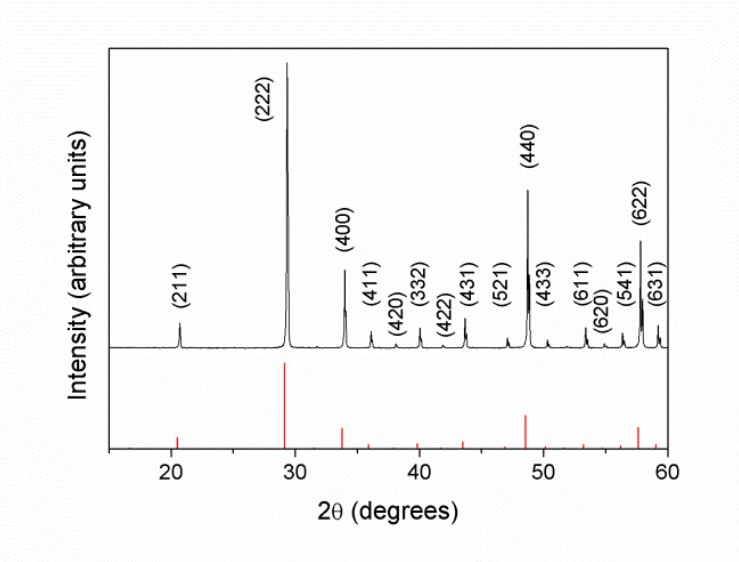

Figure 21: XRD spectrum of the pristine sample matched to the JCPDS #41-1105 profile (shown in red)

Three of the most intense diffraction peaks corresponding to the (222), (400), and (440) crystalline planes were examined for 2θ shifts. The position of these peaks in the pristine sample were at 29.373°, 34.005°, and 48.737°, respectively. Bragg's law yielded

an average lattice parameter value of 10.537Å. This lattice parameter value is 0.6% lower than the lattice parameter of 10.604Å reported by the JCPDS card for single crystal Y_2O_3. No significant deviations in the lattice parameter were observed after processing.

Density of the as fabricated ceramic was found to be 4.964g/cm^3 with a 1.7% standard deviation, in agreement with the reported values for sintered yttria [28]. Density measurements of the processed ceramic showed no statistically significant deviation from the as-fabricated ceramic.

To understand the vibrational spectra of the yttria ceramics it is first useful to discuss some structure features of Y_2O_3. The cubic structure of Y_2O_3 has space group symmetry $Ia\bar{3}$, and the unit cell is composed of 16 chemical formula units. The crystalline arrangement is composed of two yttrium-centric structures with different oxygen atom arrangements. Both arrangements are cubes with missing oxygen atoms at two corners of the cubes; one configuration has C_2 symmetry with missing oxygen atoms along a face diagonal of the cube. The other configuration, S_6, has two missing oxygen atoms along the body diagonal of the cube. The full unit cell of yttria is composed of 8 S_6 Y sites, and 24 C_2 sites, totaling in 32 cubes in the basis for the crystal structure. The symmetry type of the yttrium site determines both the regularity of the octehedra formed, as well as the Y-O bond lengths in the site. The S_6 sites form regular octahedra, with an isotropic bond length of 2.28Å (d_1). The C_2 Y sites are irregular octehedra with 3 sets of 2 Y-O pairs with lengths 2.243Å (d_2), 2.274Å (d_3), and 2.233Å (d_4). The $Y_{S6}O_6$ octahedra contact 6 of the $Y_{C2}O_6$ sites by the corners and 6 more by the edges. Conversely, the $Y_{C2}O_6$ octahedra are in contact with 2 $Y_{S6}O_6$ and 4 $Y_{C2}O_6$ octahedra at

the corners, and 6 more $Y_{C2}O_6$ octahedra at the edges. There is a reduction from 4 to 3.5Å in the Y-Y distance between octahedra linked from corner to edge [29].

The vibrational modes for yttria can be compartmentalized into two major domains roughly separated by the 300cm^{-1} frequency region. Vibrational modes in the frequency domain below the 300cm^{-1} are a result of the motions of Y atoms in the YO_6 octahedra, whereas the vibrational modes above 300cm^{-1} stem from O atoms and deformations in the YO_6 octahedra. There is a considerable amount of coupling between the different vibrations of the Y-O pairs in the two configurations described above. Figure 22 shows the ATR FTIR spectra for the as-fabricated and 10hr processed samples from 400 to 650cm^{-1}. Four absorption bands can be seen at 566, 489, 458, and 414cm^{-1}. These bands have been attributed to stretching of the YO_6 octahedra. According to a normal coordinate analysis previously published [29], the different bands possess different sensitivities to the Y-O band directionality. The bands at 566 and 489cm^{-1} are most sensitive to d_2 and d_1 Y-O vibrational modes, and have no sensitivity to d_4 vibrations or bending modes. There are additional weak couplings to the oxygen motions along the d_1 and d_2 axes in the 566cm^{-1} band that is not present in the 489cm^{-1} band. The peaks at 458 and 414cm^{-1} are highly sensitive to Y-O vibrational modes along d_4 as well as O-Y-O bending modes along the d_2 and d_1 axes. The 458cm^{-1} band lacks sensitivity to motion along the d_1 axis, and the 414cm^{-1} band lacks sensitivity to motion along the d_2 axis. Force constants for stretching modes in the 4 Y-O axes were calculated to be significantly higher in the $Y_{S6}O_6$ sites than in the $Y_{C2}O_6$ sites [29].

The absolute intensity of the bands is dependent on several experimental variables that are difficult to control, particularly the optical coupling of sample to the window of the ATR-FTIR spectrometer, but a change in relative peak intensities indicates changes in the material microstructure.

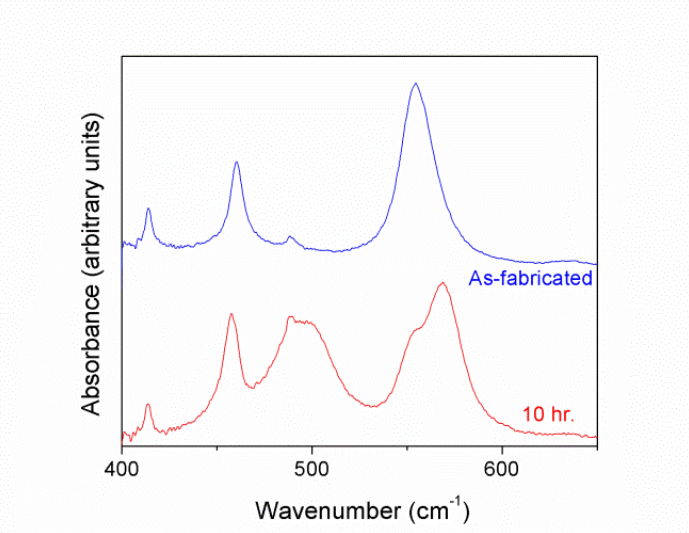

Figure 22: Partial ATR-FTIR spectra in the 400-650cm^{-1} frequency domain for the pristine and 10hr processed samples. Spectra have been overlaid for comparison

As seen in Figure 22, the relative intensity of the band at 489cm^{-1} increases dramatically compared to the 458 and 566cm^{-1} bands after thermal treatment. This is attributed to the greater ease of incorporation of oxygen in the more pliable $Y_{C2}O_6$ sites than in the rigid $Y_{S6}O_6$ sites. Since this band is related to the oxygen motion in YO_6 octahedra, the increase of the relative intensity of this band suggests oxygen uptake during the thermal processing in the O_2-rich atmosphere and thus the elimination of oxygen vacancies. Further, calculation of the force constant for the stretching modes related to the four Y-O distances discussed above shows that the S_6 octahedra are

considerably more rigid than the $Y_{C2}O_6$ octahedra [30]. Consequently, it is expected that variations in the oxygen content to be more easily accommodated in the octahedra with C_2 symmetry than one with S_6 symmetry, in agreement with the relative increase of the intensity of the band at 489cm^{-1}. Indeed, the band at 489cm^{-1} is mostly sensitive to the motion along d_2, a dependence only found in the $Y_{C2}O_6$ octahedra. The differences between the dependence of the vibrational modes on the stretching, coupled stretching, and bending along each of the *d* directions help explain why this variation is not strongly manifested in the intensity of the other bands.

The change in shape of the band at 566cm^{-1} suggests the relative intensities of two convoluted bands is changing with processing. Two peaks located at around 554 and 568cm^{-1} have been reported before[30], but never simultaneously. The structural changes causing the variation in peak intensities is not understood.

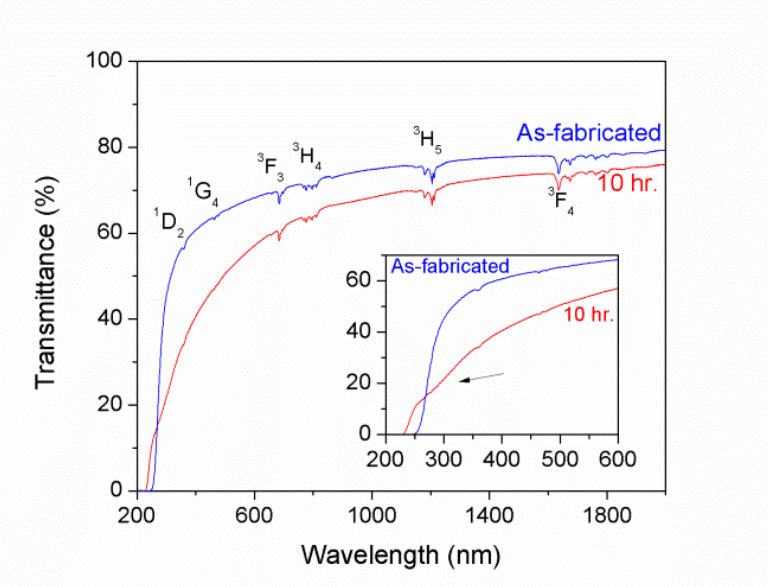

Figure 23: UV/Vis transmittance of the pristine and 10hr processed samples. Inset depicts the interstitial oxygen absorption band introduced in the sample from processing

Comparison of UV-Vis transmittance between the 10hr processed versus as-fabricated ceramic is shown above in Figure 23. The transmittance for both samples remains essentially unchanged in the near infrared region of the spectrum, remaining above 70% in agreement with [10], with some decrease in the visible range. The reason for this decrease was not identified. The absorption bands throughout the spectrum are attributed to the Tm^{3+} bands as denoted by [31]. Processing changes the transmittance primarily in the UV/Vis region outlined in the inset. There is a shift in the cut off transparency from 240 to 225nm after processing. Also, and most importantly, there is the appearance of an absorption band from 270 to 320nm that is attributed to oxygen interstitials [32].

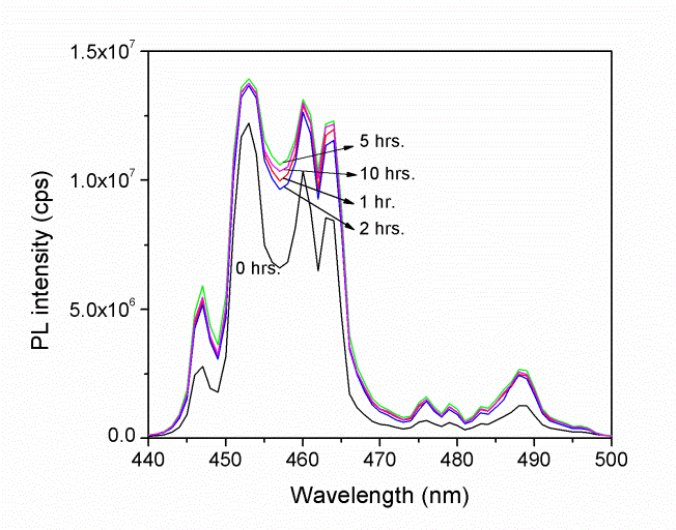

Figure 24: PL spectra of the ceramic at all processing times excited at 360nm

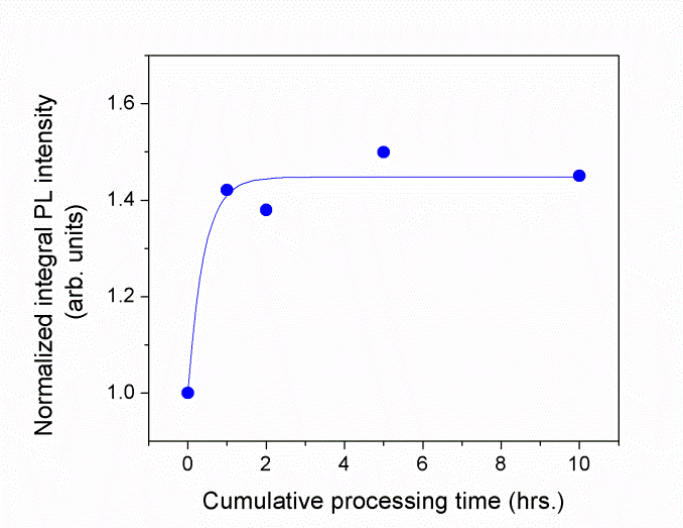

Figure 25: Normalized integral PL intensity vs. processing time, with line for eye guidance

Though the mechanisms of PL and scintillation differ, as explained below, it is useful to investigate both luminescence light yield to understand the effects of the post-

fabrication processing on the luminescent center. The PL emission band in Figure 24 is attributed to the $^1D_2$ to $^3F_4$ transitions [17]. The integral intensity plotted as a function of time can be seen in Figure 25. The integral intensity reaches a maximum of 40% PL increase after 1hr of processing, followed by satuation for longer processing times.

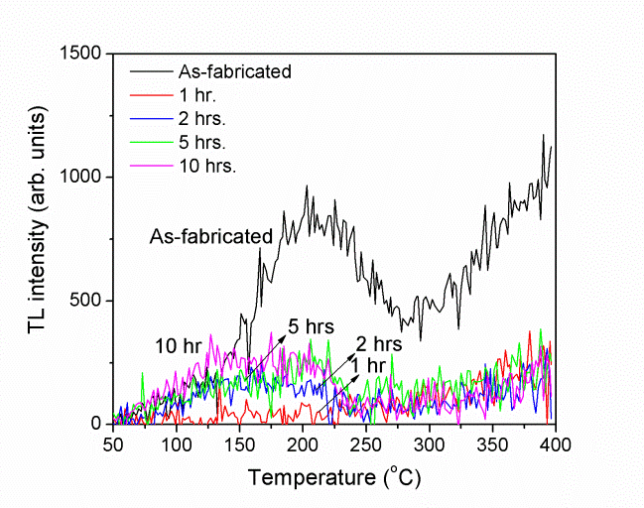

Figure 26: Thermoluminescence glow curves for all processing time

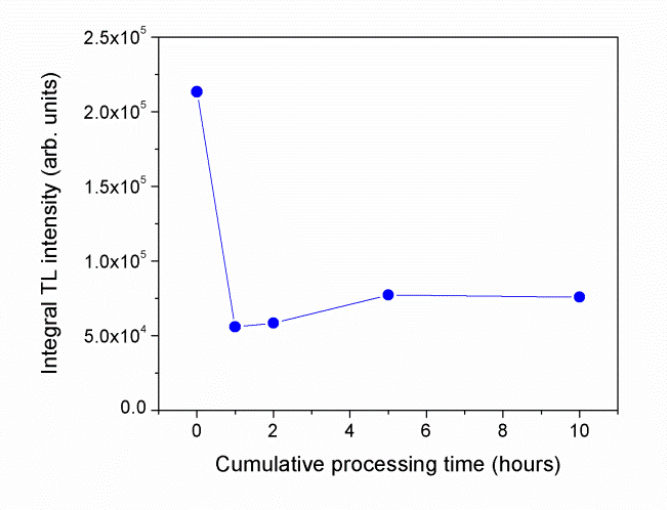

Figure 27: Integral TL intensities as a function of processing time

The TL glow curve of the as-fabricated ceramic exhibits a primary peak centered at around 210°C, with an additional increasing contribution for higher temperatures (Figure 26). Note that the difference between the glow curves in Figures 16 and 26 is the differing irradiation sources. The primary peak is shown to significantly deteriorate after 1hr of processing under oxygen. After 1hr of thermal processing in O_2 flux, the glow curve becomes featureless and greatly reduced. This reduction in integral TL intensity has been attributed to the reduction of oxygen vacancies. Further processing leads to the development of a broad band centered at about 170°C, with the integral TL intensity increasing about 30% from 2 to 5hrs of cumulative processing time, followed by stabilization at this intensity for longer processing times. The increase of integral TL intensity at longer processing times has been attributed to the introduction of oxygen interstitials into the material. The evolution of the integral TL signal is summarized in Figure 27.

TL of undoped Y_2O_3 has been performed previously, resulting in peaks at 115°C and 190°C [15], and 202°C and 353°C [33]. Accounting for the different heating rates in those reports, our peaks match those found in these sources, though the presence of additional glow peaks due to the incorporation of the Tm dopant cannot be discarded. Our data comprises the first assessment of high temperature TL of Y_2O_3:Tm as far as we are aware.

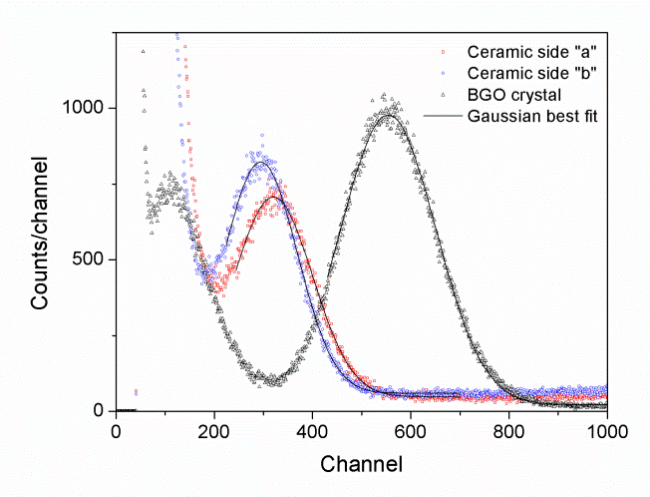

Figure 28: The results of scintillation response assessment via differential pulse height distribution measurements

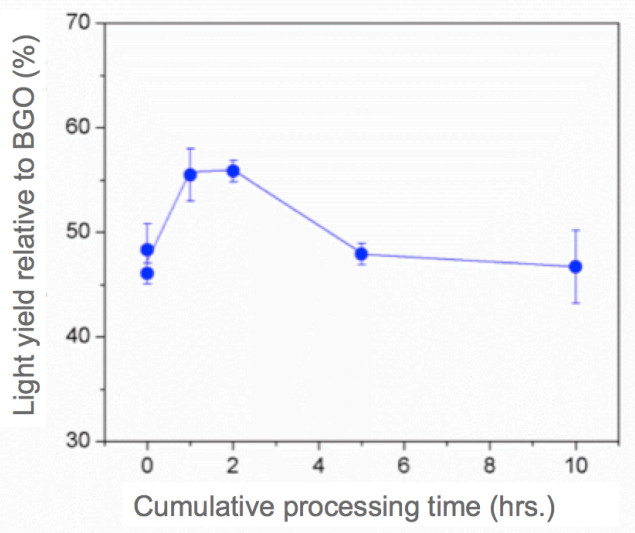

Figure 29: Light yield relative to BGO vs. thermal processing time

The photopeak centroids for the 60keV ^{241}Am gamma rays with the ceramic are located at channels 295 and 320 for both sides of the ceramic, and channel 554 for the BGO crystal reference (Fig. 28). A weak peak in the distribution from the BGO crystal is attributed to the low energy X-ray emissions from the ^{241}Am source/daughter product ^{237}Np, but this peak is not used to assess the light yield of the scintillators. As discussed in section 2.2.8, the scintillator brightness is correlated to the channel number of the photopeak; the higher the peak channel number, the brighter the material. We observe a 20% increase in the light yield of the ceramic relative to the BGO reference within the first hour of processing, followed by saturation at the enhanced value through 2hrs of processing. Further processing results in a decrease in the light yield of the sample relative to BGO, returning to roughly the pre-processing intensity, as shown in Figure 29.

It is shown that the first hour of thermal processing under O_2 flow leads to higher light yield, lower integral TL intensity, higher PL integral intensity. After the total cumulative processing time, the decrease in light yield, increase in TL intensity, and introduction of the 270-350nm absorption band are noted. In fact, comparison between TL and light yield results suggest them to be related. The appearance of the 270-350nm absorption band in the UV-Vis absorption spectrum shows that after the entire processing time, oxygen was incorporated in the form of interstitials. It seems reasonable to admit that oxygen was first incorporated in the native vacancies of the host, and that the sample was fully processed by the 1-2hr mark, and further thermal treatment resulted in exceeding the equilibrium oxygen vacancy prevalence with subsequent incorporation of oxygen interstitials.

It is important to note that the PL intensity at higher processing times stabilizes as opposed to changing like the other quantities being examined. This is a result of the difference between the scintillation and PL mechanisms. PL involves direct excitation of the Tm^{3+} luminescence centers and does not entail electron transport through the host, in opposition to the case of scintillation. This implies that PL intensity is less dependent of the existence of defects, with the exception of defects within the close vicinity of the luminescence center. Scintillation, on the other hand, will be much more affected by defects anywhere in the host because the scintillation process involves the transport of electrons and holes through the material until they recombine at a luminescence center. During this transport, they can be captured by traps created by these defects, decreasing the overall efficiency of the scintillation process.

4 – Conclusion/Future Work

An investigation of the effects of thermal post-fabrication processing on the scintillation, optical, and microstructural characteristics of transparent Y_2O_3:Tm ceramics was performed for the first time. Further, investigation of sintering effects on the densification and trap content in Y_2O_3 was carried out. To the best of our knowledge, it is the first attempt to correlate fabrication conditions and trap content in Y_2O_3. Sintering reduces the defect content of Y_2O_3, but the defect prevalence increases with increasing sintering temperature. The results indicated that thermal O_2 processing of Y_2O_3:Tm can improve the performance of the ceramics, if processed for the right duration. The optimal processing duration seems to be 1 to 2hrs, which leads to about 40% enhancement in the photoluminescence and about 20% enhancement in the scintillation light yield. The enhancement in these properties was tentatively attributed to the incorporation of oxygen in vacancy sites. Beyond the 2hr processing time, the deterioration of scintillation properties are attributed to the introduction of interstitial oxygen. These results suggest post-fabrication thermal processing under O_2 flow to be an effective method for improving scintillation properties of transparent ceramics.

Results of this work have been accepted for publication in Journal of Luminescence titled "Luminescence and scintillation enhancement of Y_2O_3:Tm transparent ceramic through post-fabrication thermal processing" by M.G. Chapman, M.R. Marchewka, S.A. Roberts, J.M. Schmitt, C. McMillen, C.J. Kucera, T.A. DeVol, J. Ballato and L.G. Jacobsohn.

Further work involves a detailed examination of what happens within the first 2hrs of processing, together with the analysis of TL results in order to clarify the mechanisms involved in enhancing the scintillation performance of transparent ceramics.

Work Cited

[1] S. A. Dyer, "Survey of instrumentation and measurement," *Wiley-IEEE,* p. p. 920, 2001.

[2] W. R. Leo, "Techniques or Nuclear and Particle Physics Experiments," 1994.

[3] R. Hofstadter, "US patent 2585551 "Means for detecting ionizing radiations"," 1948.

[4] C. W. E. van Eijk, "Development of inorganic scintillators," *Nuclear Inst. and Methods in Physics Research, A,* vol. 392, pp. 285-290, 1997.

[5] C. W. E. v. Eijk, "Inorganic scintillators in medical imaging," *Physics in Medicine and Biology,* vol. 47, p. R85, 2002.

[6] C. Greskovich and S. Duclos, "CERAMIC SCINTILLATORS," *Annual Review of Materials Science,* vol. 27, pp. 69-88, 1997.

[7] S. N. Ahmed, *Physics and engineering of radiation detection*. Amsterdam: Academic Press, 2007.

[8] J. J. Swab, Widjaja, Sujanto, Singh, Dileep, *Advances in Ceramic Armor VII : Ceramic Engineering and Science Proceedings*. Hoboken: Wiley-American Ceramic Society, 2011.

[9] V. Lupei, A. Lupei, and A. Ikesue, "Transparent polycrystalline ceramic laser materials," *Optical Materials,* vol. 30, pp. 1781-1786, 2008.

[10] J. Li, Y. Pan, Y. Zeng, W. Liu, B. Jiang, and J. Guo, "The history, development, and future prospects for laser ceramics: A review," *International Journal of Refractory Metals and Hard Materials,* vol. 39, p. 44, 2013.

[11] D. Djurovic, M. Zinkevich, and F. Aldinger, "Thermodynamic modeling of the yttrium–oxygen system," *Calphad,* vol. 31, pp. 560-566, 12// 2007.

[12] S. Karn, K. Baris, Y.-K. Basak, K. Marian, and B. John, "Synthesis, Processing, and Properties of Submicrometer-Grained Highly Transparent Yttria Ceramics," *American Ceramic Society. Journal of the American Ceramic Society,* vol. 93, p. 1320, 2010.

[13] Y. Ato, R. Huzimura, and L. Ozawa, "Gamma-Ray Thermoluminescence in Rare-Earth-Activated Y2O3Phosphors," *Japanese Journal of Applied Physics,* vol. 7, pp. 1497-1503, 1968.

[14] Y. Nigara, "Measurement of the Optical Constants of Yttrium Oxide," *Japanese Journal of Applied Physics,* vol. 7, pp. 404-408, 1968.

[15] M. S. Jahan, D. W. Cooke, W. L. Hults, J. L. Smith, B. L. Bennett, and M. A. Maez, "Thermally stimulated luminescence from commonly occuring impurity phases in high-temperature superconductors," *Journal of Luminescence,* vol. 47, pp. 85-91, 1990.

[16] N. Garnier, R. Moncorge, H. Manaa, E. Descroix, P. Laporte, and Y. Guyot, "Excited-state absorption of Tm3+-doped single crystals at photon-avalanche wavelengths," *Journal of Applied Physics,* vol. 104, pp. 4323-4329, 1996.

[17] F. S. Ermeneux, C. Goutaudier, R. Moncorgé, M. T. Cohen-Adad, M. Bettinelli, and E. Cavalli, "Growth and fluorescence properties of Tm 3+ doped YVO 4 and Y 2O 3 single crystals," *Optical Materials,* vol. 8, pp. 83-90, 1997.

[18] J. Mun, T. Fukuda, A. Jouini, A. Novoselov, Y. Guyot, A. Yoshikawa*, et al.*, "Growth and characterization of Tm-doped Y2O3 single crystals," *Optical Materials,* vol. 29, pp. 1390-1393, 2007.

[19] W. Li, S. Zhou, H. Lin, H. Teng, N. Liu, Y. Li*, et al.*, "Controlling of Grain Size with Different Additives in Tm3+:Y2O3 Transparent Ceramics," *Journal of the American Ceramic Society,* vol. 93, pp. 3819-3822, 2010.

[20] H. Yihua, J. Dongliang, Z. Jingxian, L. Qingling, and H. Zhengren, "Sintering of Transparent Yttria Ceramics in Oxygen Atmosphere," *American Ceramic Society. Journal of the American Ceramic Society,* vol. 93, p. 2964, 2010.

[21] B. Y. K. K. Serivalsatit, B. Kokuoz, J. Ballato, *Opt. Lett.,* vol. 34, p. 1033, 2009.

[22] J. Hao, S. A. Studenikin, and M. Cocivera, "Blue, green and red cathodoluminescence of Y2O3 phosphor films prepared by spray pyrolysis," *Journal of Luminescence,* vol. 93, pp. 313-319, 2001.

[23] P. Y. Poma, K. U. Kumar, M. V. D. Vermelho, K. Serivalsatit, S. A. Roberts, C. J. Kucera*, et al.*, "Luminescence and thermal lensing characterization of singly Eu3+ and Tm3+ doped Y2O3 transparent ceramics," *Journal of Luminescence,* vol. 161, pp. 306-312, 2015.

[24] A. Nordmann, "Refraction on an apeture - Huygens-Fresnel principle," 2007.

[25] Y. Leng, "Materials Characterization Introduction to Microscopic and Spectroscopic Methods," 2008.

[26] K. G. L. P. Asoka-Kumar, and D.O. Welch, "Characterization of Defects in Si and SiO2-Si using Positrons," 1994.

[27] J. Kansy, *Instr. Meth. Phys. Res.* , vol. 374, p. 235, 1996.

[28] O. Yeheskel and O. Tevet, "Elastic Moduli of Transparent Yttria," *Journal of the American Ceramic Society,* vol. 82, pp. 136-144, 1999.

[29] Y. Repelin, C. Proust, E. Husson, and J. M. Beny, "Vibrational Spectroscopy of the C-Form of Yttrium Sesquioxide," *Journal of Solid State Chemistry,* vol. 118, pp. 163-169, 1995.

[30] J. A. K. G. Schaack, *J. Opt. Soc. Am.,* vol. 60, p. 1110, 1970.

[31] R. P. Leavitt, "Optical spectra, energy levels, and crystal-field analysis of tripositive rare-earth ions in Y2O3. II. Non-Kramers ions in C2 sites," *The Journal of Chemical Physics,* vol. 76, p. 4775, 1982.

[32] W. Van Schaik and G. Blasse, "Influence of defects on the luminescence quantum yield of yttrium europium oxide (Y1.94Eu0.06O3)," *Chemistry of Materials,* vol. 4, pp. 410-415, 1992.

[33] B. N. Lakshminarasappa, J. R. Jayaramaiah, and B. M. Nagabhushana, "Thermoluminescence of combustion synthesized yttrium oxide," *Powder Technology,* vol. 217, pp. 7-10, 2012.